

*Full Paper*

## **Hybrid framework for 3D colon model reconstruction from computed tomographic colonography**

**Pataraporn Promkumtan<sup>1</sup>, Nagul Cooharajanone<sup>1, \*</sup>, Rajalida Lipikorn<sup>1</sup>, Laddawan Vajragupta<sup>2</sup> and Bundit Chaopathomkul<sup>2</sup>**

<sup>1</sup> Department of Mathematics and Computer Science, Faculty of Science, Chulalongkorn University, Thailand

<sup>2</sup> Department of Radiology, Faculty of Medicine, Chulalongkorn University, Thailand

\* Corresponding author, e-mail: [Nagul.C@chula.ac.th](mailto:Nagul.C@chula.ac.th)

*Received: 10 December 2013 / Accepted: 13 March 2015 / Published: 16 March 2015*

---

**Abstract:** A hybrid framework for an improved resolution of 3D-model colon reconstruction from computed tomographic colonography images is proposed. The framework is composed of three main parts: colon cleansing, colon-wall detection and colon segmentation followed by 3D model reconstruction. The first part, colon cleansing, was performed by applying a Laplacian operator combined with K-means clustering and morphological-based operations. An average Gaussian low-pass filter of two different sizes combined with a median filter was employed to reconstruct the colon wall as realistically as possible, and was evaluated on four data sets by an expert radiologist. The second part, colon-wall detection, utilised hybrid edge and enhanced gradient vector flow procedures to enhance the colon-wall detection, and the results were evaluated on eight data sets in comparison with two existing techniques by two expert radiologists. Finally, colon segmentation, based on anatomical structures and volume analysis, was applied and then 3D models were reconstructed. The colon cleansing was consistent across all data sets and gave satisfactory removal of all partial volume effects and contrast-enhancing material, whilst the proposed method gave better results for colon wall segmentation than the existing methods, even in special cases of unusually structured colons.

**Keywords:** computed tomographic colonography, colorectal cancer, polyps, colon cleansing, colon detection

---

### **INTRODUCTION**

Colorectal cancer is a deadly disease in both men and women if the pathological symptoms are not diagnosed in the early stages [1]. Most colorectal cancers can be successfully treated if the pre-cancer cells (polyps) are detected and diagnosed at an initial stage. Virtual colonoscopy, also

called computed tomographic (CT) colonography, is used in colorectal cancer screening, which is performed by scanning the patient's abdomen to produce a series of cross sectional CT colonography images. This non-invasive technique is more comfortable for patients because they do not need a physical cleansing, which is comprised of either cleansing the colon with a large volume of liquids or taking medication and enemas to clear the colon lumen. Instead, the patient orally takes a contrast enhancement agent to make the retained residual materials (faeces and liquid stool) inside the colon radio-opaque so that they can be removed from the CT images by computerised cleansing [2].

However, CT colonoscopy has two main problems. The first is in cleaning up the colon images (colon cleansing) to eliminate any retained material of contrast-enhancing fluid (CEF) inside the colon lumen for reliable and accurate polyp detection. Although the intensities of these unwanted residual materials are enhanced, they do not show explicit boundaries due to the partial volume effect (PVE). Therefore, although applying simple threshold subtraction on the residual materials gives the fastest result, it cannot eliminate the PVE voxels at the interface region between the residual fluids and air, and it also increases aliasing effects at the surface of the colon wall.

The second problem is in the colon-wall detection and segmentation stage. The accuracy of the colon-wall detection is important in localising and identifying the size of polyps, but artefacts such as blurred surfaces where the colon lumen meets with air can reduce the accuracy of the colon-wall detection. Moreover, the colon is not the only air-filled organ in the abdomen. The lower portion of the lung, as well as the stomach and intestine are sometimes present in CT images. These air-filled organs make the task of accurate colon segmentation more difficult.

Many techniques for colon cleansing and PVE removal were reported previously. Typically, learning vector quantisation was applied for image classification and colon cleansing [3] whilst threshold value selection (based on the histogram of all the data intensity) and vertical filter were utilised for removing the CEF and PVE boundary [4]. However, these techniques did not address the effect of the sharpened intensity at the mucosal layers after colon cleansing. Segmentation ray casts with volume intensity distribution have been used to define the profile pattern for detecting the PVE whilst reconstruction graphs have been employed for removing the residuals [5]. Moreover, non-linear transfer function and morphological dilation operations have been used to find the intensity profile of the CEF [6] whilst a threshold function combined with triangular intensity transformation has been used for colon cleansing [7]. Similarly, half-sized data have been applied for generating the local and global histograms of the CEF to make a binary mask and then a morphological dilation operation is applied to seed the region growing [8]. Nevertheless, these methods require cautious selection of the optimal intensity for assigning the classification tasks.

Various techniques on automated colon-wall detection and segmentation have been developed. Although the basic techniques usually apply region growing [4, 8-9], these methods suffer from a limited capacity to find the optimal threshold setting and require refinement of the colon border. Another approach is to use the immersion-based watershed algorithm to compute the colon lumen border using a gradient map [6, 10-11]. Nevertheless, this method also has restrictions on their resolution of the complex contours of the colon border. Although level-set methods [12-15] have been used for colon segmentation, the identification of the decreasing shade intensity voxels on the border of the colon wall and the concave regions is still problematic. The traditional deformable model has the limitation of a small capture range and also has difficulties in driving into the concave boundary regions [16, 17]. Consequently, a gradient vector flow (GVF) deformable model has been developed to give a greater capture range in driving into concave regions [18, 19] in many

medical image segmentations [20-24]. However, the blurred area of low-intensity shading at the border of the colon wall still makes the edge detection difficult by the traditional GVF method.

For these reasons, we propose a hybrid framework for colon cleansing and colon-wall detection and segmentation to solve the described problems and to reconstruct a 3D colon model as realistically as possible. This will encourage radiologists to improve the diagnostic performance when performing a fly-through (the movement of virtual viewing inside colon) and displaying the entire 3D colon model with accurate surface and shape of colon. The proposed framework is composed of three main parts (Figure 1) and described as follows.

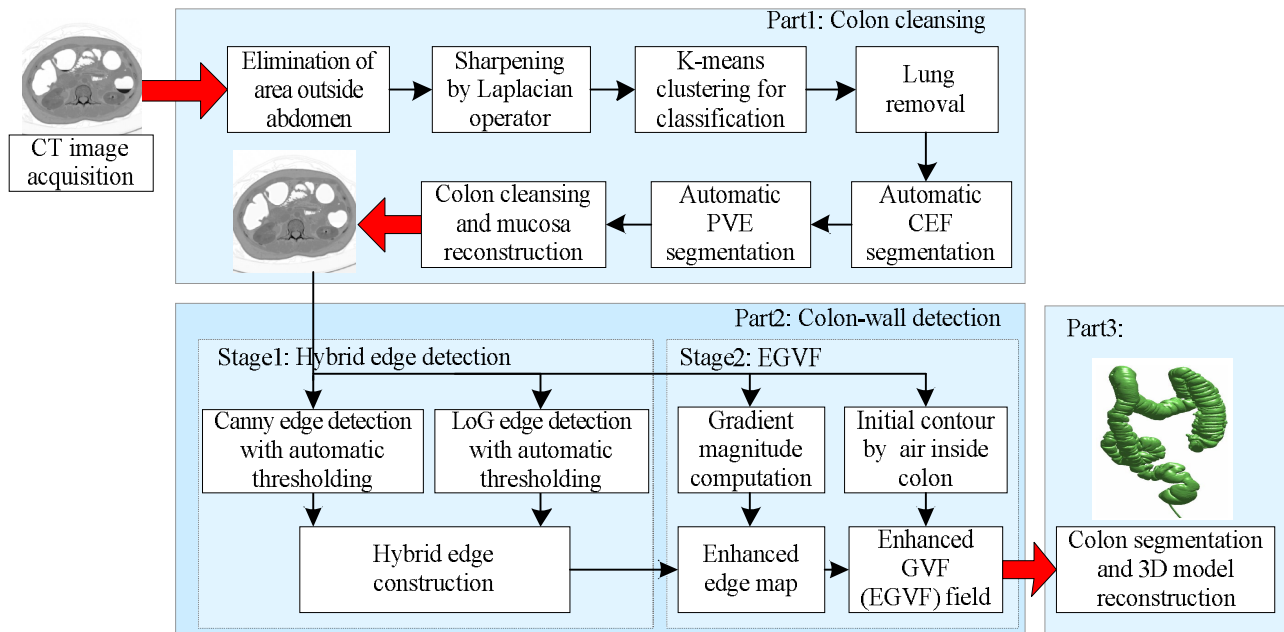


**Figure 1.** Proposed hybrid framework for colon cleansing and colon-wall detection and segmentation

The first part is the colon cleansing process, which uses a Laplacian operator combined with K-means clustering [25] to detect and eliminate the CEF and then applies morphological operations to remove the undesirable PVE. Moreover, the mucosal layers are reconstructed by an average Gaussian low pass filter of two different sizes combined with a median filter.

The second part is the colon-wall detection process, which uses an enhanced gradient vector flow (EGVF) to assist in the detection of the colon lumen. The proposed EGVF algorithm is composed of two stages. The first stage is the calculation of the hybrid edge, which is performed by combining the edge derived from the Canny edge detector [26] with automatic thresholding and that from the Laplacian of Gaussian (LoG) detectors [27] with automatic thresholding. In the second stage, the derived hybrid edge is then used as an edge mask to construct an enhanced edge map. This map is then applied to generate the EGVF for the detection of the colon wall.

The third part is the colon segmentation and 3D model reconstruction. The colon segmentation method is based on the anatomical structure of the colon and a volume analysis for the rendering of a 3D colon model.

## MATERIALS AND METHODS

### CT Image Acquisition and Elimination of Area Outside Abdomen

Since the retained faeces in the colon lumen can conceal polyps, all patients must undergo a standard bowel preparation involving a low-residue diet and take colonic lavage to make the retained faeces become more liquid. A contrast-enhancing agent such as barium sulphate was then taken to make the residual fluid radio-opaque and then the colon lumen was inflated to distend the colon and also to homogenise the residual material. After that, the CT colonographic scan was performed by a spiral CT scanner (Siemens SOMATOM Sensation 16, Technical Prospects, LLC, USA) to produce CT colonographic images. The acquired images were constructed at 1-mm intervals with 512×512 voxels, resulting in 500-700 slices. This approach had been approved by the Ethics Committee of the Faculty of Medicine, Chulalongkorn University.

The voxels outside the body were automatically detected and were discarded from the CT images in order to eliminate the extra computing time. The Otsu's method [28] was applied to separate the CT image into the foreground and the background. Afterwards, the areas outside the abdomen were discarded and all voxels inside the abdomen were preserved for the next process.

### Image Sharpening by Laplacian Operator

Traditional K-means clustering is not precise at separating voxels that are located between two transitional regions and so small artifacts of CEF can be missed. Thus, the images were sharpened by Laplacian operator [27] via the highlighting of the discontinuity intensity levels. The sharpened image  $I_{sh}(x,y)$  was acquired from Eq. (1):

$$I_{sh}(x,y) = I(x,y) - \nabla^2 I(x,y), \quad (1)$$

where  $\nabla^2$  is the Laplacian operator and  $I(x,y)$  is a CT image slice at coordinates  $x$  and  $y$ .

### K-means Clustering for Colon Classification

Although applying thresholding is the simplest method in segmentation, each range of threshold intensities is sensitive to the intensity inhomogeneity. A slight change to these threshold values can affect the contour of colon, especially the thin tissue layers that may then disappear. Thus, it is not easy to select proper threshold intensities, and for this reason K-means clustering was applied to assist in image classification since the number of clusters for partitioning the regions is known and it converges to the optimal solution faster than the other pixel-based methods [25].

The intensity of each sharpened image was then used as feature vector  $X = \{x_i | i = 1, 2, 3, \dots, n\}$  to classify into four main regions of (i) air, (ii) soft tissue and fat, (iii) muscle, and (iv) contrast-enhanced material and bones. The algorithm of K-means clustering was started by initialising the centroid of each cluster  $z_1, z_2, z_3$  and  $z_4$  at random from a range of data. At the  $p^{\text{th}}$  iteration, the feature vector  $x_i$  was assigned to the respective cluster  $C_j$  ( $j = 1, 2, 3$  or  $4$ ) whose centroid was the nearest or whose Euclidean distance was the minimum, as expressed in Eq. (2):

$$x_i \in C_{j,p} \text{ if } \|x_i - z_{j,p}\| < \|x_i - z_{k,p}\|, \quad (2)$$

where  $\|\cdot\|$  represents the Euclidean distance function,  $C_{j,p}$  denotes a cluster  $j$  at the  $p^{\text{th}}$  iteration whose centroid is  $z_{j,p}$ , and  $k = 1, 2, 3$  or  $4$  with the condition that  $j \neq k$ . Afterwards, the new centroid of each cluster,  $z_{j,p+1}$  in the  $p+1^{\text{th}}$  iteration, was recalculated to minimise the criterion function, as in Eq. (3)

$$J = \sum_{i=1}^{N_j} |x_{i,j} - z_{j,p+1}|, \quad (3)$$

where  $x_{i,j}$  is in  $C_j$  and  $N_j$  is the number of voxels of cluster  $j$ . The value of  $z_{j,p+1}$  which can minimise this criterion became the new centroid of the cluster and was computed by Eq. (4);

$$z_{j,p+1} = \frac{1}{N_j} \sum_{i=1}^{N_j} x_i, \quad (4)$$

The algorithm terminates if the centroids have not changed; otherwise, it will return to recalculate the clusters. To find the global minimum, several replications with random starting centroids were applied in order to converge the solutions to a global minimum. A sample image before and after performing K-means clustering is shown in Figures 2(a) and 2(b) respectively.

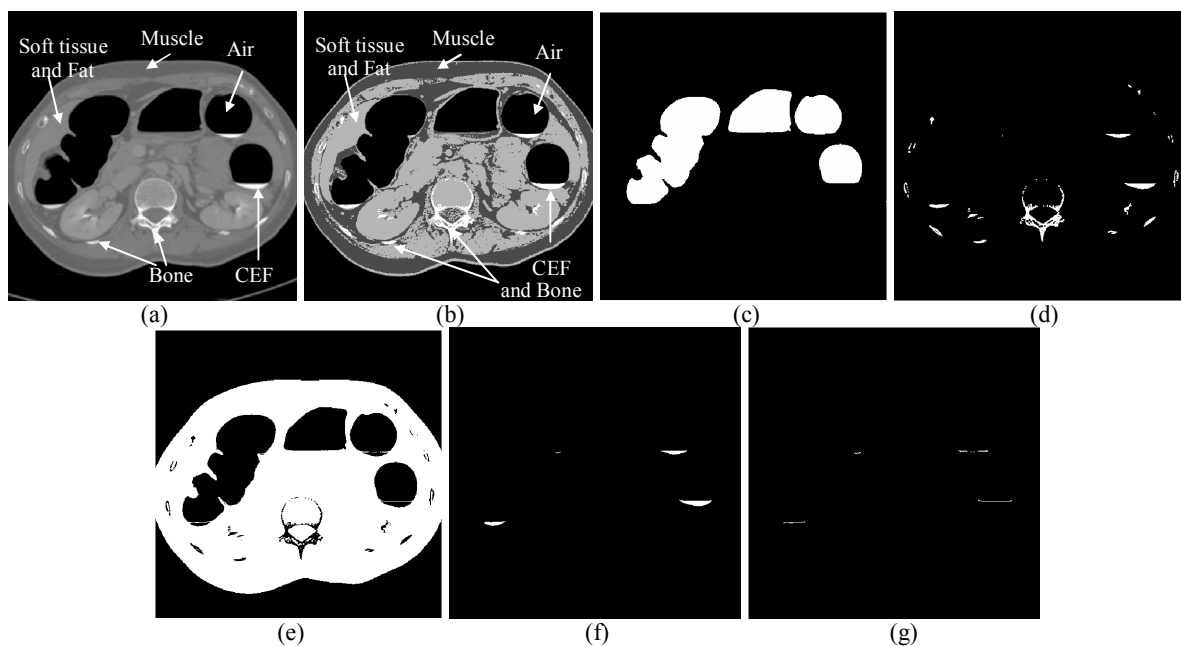


**Figure 2.** Original CT image slice (a) and that after K-means clustering (b), plus  $Mask_{Air}$  (c),  $Mask_{CEF-Bone}$  (d),  $Mask_{Tissue}$  (e);  $Mask_{CEF}$  (f) and  $Mask_{PVE}$  (g)

### Lung Removal

The prior removal of lungs was employed to eliminate the extra computation. Traditionally, a threshold setting is used to separate the lung tissue. In contrast, here the lungs were removed based upon their anatomical characteristic (they contain many blood vessels). Preliminarily, the air regions were constructed with a binary mask and labelled as  $Mask_{Air}$ . If a segment of  $Mask_{Air}$  had holes inside, assumed to be blood vessels, it was designated as lung and ignored (Figure 3).

### Automatic CEF Segmentation

The region of CEF and the bones were defined as  $Mask_{CEF-Bone}$  (Figure 2(d)), whilst the regions of soft tissues and muscles were combined together and called  $Mask_{Tissue}$  (Figure 2(e)). Since the CEF was concentrated at the lower part of the colon due to gravity and also appeared between the colon wall and the air region, then the voxels that surround the  $Mask_{CEF-Bone}$  were examined for these restrictions to distinguish the CEF from bone and denoted as  $Mask_{CEF}$  (Figure 2(f)).

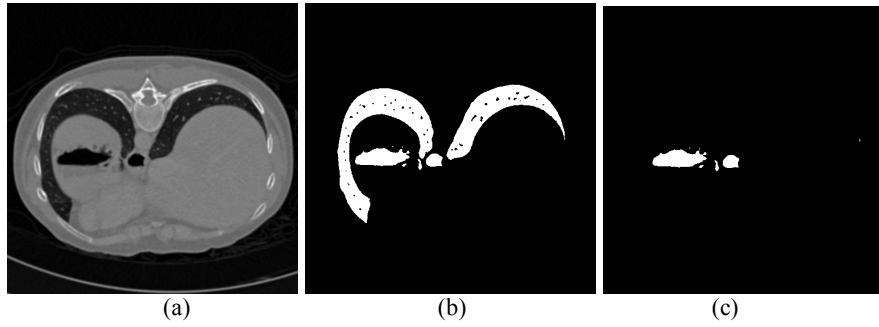


**Figure 3.** CT image slice (a) and that for  $Mask_{Air}$  before lung removal (b) and after lung removal (c)

### Automatic PVE Segmentation

The PVE between air and CEF still remained in the  $Mask_{Tissue}$ . Then the boundary that included the interface layer of PVE voxels, assigned as  $Mask_{Merge}$ , was calculated by merging the boundaries of dilated masks of each segment of  $Mask_{CEF}$  and their contiguous  $Mask_{Air}$  with OR operation and applying morphological erosion afterwards, as in Eq. (5):

$$Mask_{Merge} = ((Mask_{Air,i} \oplus s_e) \vee (Mask_{CEF,i} \oplus s_e)) \ominus s_e, \quad (5)$$

where  $\oplus$  and  $\ominus$  represent the morphological dilation and erosion respectively, with a disk-shaped structuring element  $s_e$  whose radius size was equal to one.  $Mask_{CEF,i}$  is each segment of  $Mask_{CEF}$ ,  $Mask_{Air,i}$  is a segment of  $Mask_{Air}$  that is contiguous to  $Mask_{CEF,i}$ , and  $i$  represents each colon segment that has CEF. The symbol  $\vee$  represents the OR operation. The suspected PVE that interfaced between the air and CEF, called  $Mask_{TestPVE}$ , was obtained by using the AND operation on  $Mask_{Merge}$ ,  $Mask_{Tissue}$  and the dilation of each segment of  $Mask_{CEF}$ , as given in Eq. (6):

$$Mask_{TestPVE} = Mask_{Merge} \wedge Mask_{Tissue} \wedge (Mask_{CEF,i} \oplus s_e), \quad (6)$$

where  $\wedge$  represents the AND operation.

Since there are two possible types of each component of  $Mask_{TestPVE}$  (soft tissue or PVE), the inspection was performed with the assumptions that the PVE voxels were the interface layer appearing between the air and CEF; otherwise they were defined as tissue. Eventually, the PVE regions was determined and labelled as  $Mask_{PVE}$  (Figure 2(g)).

### Colon Cleansing and Mucosa Reconstruction

The dilated  $Mask_{PVE}$  and  $Mask_{CEF}$  were combined together and then subtracted from the CT image, successfully eliminating the CEF and PVE voxels. Consequently, the reconstructed edge of the mucosal layer was generated on the adjacent pixels of the removed edge and denoted as  $Edge_i$ , where  $i$  is the adjacent pixels of the removed edge. Then the estimated intensity value of each voxel of  $Edge_i$  was calculated, as in Eq. (7):

$$I_{Edge,i} = (I_{G5,i} + I_{GM3,i})/2, \quad (7)$$

where  $I_{Edge,i}$  is the intensity value of each voxel of  $Edge_i$ ,  $I_{G5,i}$  is the intensity value at each voxel of  $Edge_i$  after convolving the cleaned colon image by a Gaussian low-pass filter with a  $5 \times 5$  voxels mask size, and  $I_{GM3,i}$  is the intensity value at each voxel of  $Edge_i$  after convolving the cleaned colon image by a Gaussian low-pass filter with a  $3 \times 3$  voxels mask size and then performing median filtering to eliminate some noises of inharmonious intensity. Subsequently,  $I_{Edge,i}$  was calculated and replaced on the  $Edge_i$  to give a more natural appearance of the mucosal layer. From the experiment,

the Gaussian filter of both sizes could be applied to 512×512 voxels (standard size of CT image) and a larger or smaller size of this image. A larger mask size made the image more blurred whilst a smaller mask size could not completely reduce the effect of the rapid transition of the intensity level. However, the mask size of the Gaussian filter should not be more than 5×5 voxels since the intensity at the reconstructed edge areas would be obviously different from the surrounding tissue layers. Even if the median filter could remove noise, it should not be used with a smaller image size since it might cause the omission of small protrusions in the tissue layers.

### Hybrid Edge Detection

The algorithm of the hybrid edge detection method was composed of three stages: (i) Canny edge detection [26] with automatic threshold setting, (ii) LoG edge detection [27] with automatic threshold setting, and (iii) hybrid edge construction. These are described in turn below.

#### *Canny edge detection with automatic threshold setting*

The gradient magnitude of the cleaned colon image was calculated. Afterwards, a non-maximum suppression was performed to track along the top of the ridges so that only the gradient magnitudes at the points of the greatest local change were identified. Hysteresis was then applied to track the edges and eliminate broken edges and streaks. Hysteresis as implemented here depended on the setting scale of the two thresholds,  $T_1$  and  $T_2$ , for detecting the edge location. The value of threshold  $T_1$  was automatically selected utilising Otsu's method [28], which is normally used with the intensity values of the CT image, but here the gradient magnitude of the cleaned colon image was applied instead. Then the between-class variance was determined from Eq. (8):

$$\sigma_b^2 = w_{g1}[\mu_{g1} - \mu_{gT}]^2 + w_{g2}[\mu_{g2} - \mu_{gT}]^2. \quad (8)$$

where  $w_{g1}$  and  $w_{g2}$  are the probability distribution of the gradient magnitude value on the foreground and background respectively,  $\mu_{g1}$  and  $\mu_{g2}$  are the mean gradient magnitudes of the foreground and background respectively, and  $\mu_{gT}$  is the net mean gradient magnitude. The threshold which corresponded to the maximum between-class variance was defined as  $T_{Otsu}$ . The threshold  $T_1$  for hysteresis was set to equal to  $T_{Otsu}$ , whilst  $T_2$  was then calculated from Eq. (9):

$$T_2 = kT_{Otsu} = kT_1, \quad (9)$$

where  $k$  is a scaling factor which makes  $T_2 < T_1$  (in this case  $k = 0.4$ ) in order for the weak edges to be detected. When the gradient magnitude was greater than the  $T_1$ , it was identified as a strong edge, and when it was between  $T_1$  and  $T_2$ , it was identified as a weak edge, unless there was a connecting path from the weak edge pixels to the strong edge pixels, in which case edge linking was then performed. The derived edges were then labelled as  $f_C$ . A sample result is shown in Figure 4(b).

#### *LoG detection with automatic threshold setting*

The cleaned colon image was smoothed by the use of a Gaussian filter and subsequently the LoG was calculated as the second spatial derivative of the smoothed image. Zero-crossing detection was utilised to estimate the edge locations. The threshold value for the zero-crossing operation,  $T_z$ , was automatically set by the mean absolute value of LoG, as derived from Eq. (10):

$$T_z = \frac{1}{mn} \sum_{x=1}^m \sum_{y=1}^n |LoG(x, y)|, \quad (10)$$

where  $LoG(x,y)$  is the intensity level estimated by the LoG image at coordinates  $(x, y)$  of an image whose size is  $m \times n$ . The derived edges were then labelled as  $f_{LoG}$ . A sample result is shown in Figure 4(c) in grey and white. Afterwards, the LoG edges located at positions where the gradient magnitude was greater than  $T_{Otsu}$  were preserved; otherwise they were removed as noisy edges. Hence the final LoG edges were acquired by Eq. (11):

$$f_{LoG}(x,y) = \begin{cases} f_{LoG}(x,y) & \text{if } f_G(x,y) \geq T_{Otsu} \\ 0 & \text{if } f_G(x,y) < T_{Otsu} \end{cases}, \quad (11)$$

where  $f_G(x,y)$  is the gradient magnitude of an image at coordinates  $(x, y)$ . A sample image of LoG edges after elimination of the noisy edges is shown in Figure 4(c) in white.

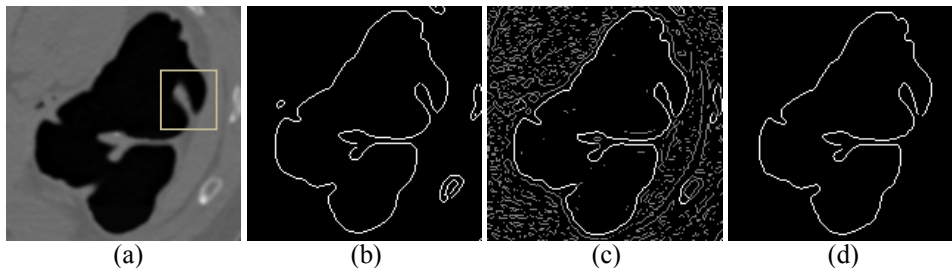


**Figure 4.** (a) Original CT image slice; (b) after Canny edge detection by automatically-set threshold; (c) after LoG edge detection by automatically-set threshold (white) and discarded edge (grey); (d) hybrid edge obtained by (b) and (c)

#### Hybrid edge construction

Although the Canny edge detection could produce strong edges, it identified an edge without examining the deviations from its neighbours [29]. In contrast, the LoG edge detection defined the edge by examining an area nearby each pixel, but it was sensitive to noise [30, 31]. Consequently, the hybrid edge derived from both detectors could assist in edge localisation and noise reduction better than that from either detector alone. Only the edges obtained from both methods and contiguous to the air inside the colon were conserved, whilst those at the other locations were eliminated. If the edges detected by both detection were at the same location, they were preserved for the hybrid edges and assigned as  $f_{Hyb}$ . The remaining segments in the Canny edge and LoG edge images which were not preserved were called  $S_{Canny}$  and  $S_{LoG}$  respectively. Each segment of  $S_{LoG}$  and  $S_{Canny}$  which were contiguous to  $S_{LoG}$  was then analysed by Eqs. (12) and (13) respectively:

$$E_{LoG} = \sum_{i=i_0}^{i_{n-1}} \sum_{j=j_0}^{j_{n-1}} \frac{I_{LoG}(i,j)}{n}, \quad (12)$$

$$E_{Canny} = \sum_{k=k_0}^{k_{m-1}} \sum_{l=l_0}^{l_{m-1}} \frac{I_{Canny}(k,l)}{m}, \quad (13)$$

where  $n$  and  $m$  are the numbers of pixels of each segment of  $S_{LoG}$  and  $S_{Canny}$  respectively. The notation  $I_{LoG}(i,j)$  represents the intensity of each pixel of  $S_{LoG}$  at coordinates  $i$  and  $j$ . Similarly,  $I_{Canny}(k,l)$  is the intensity of each pixel of  $S_{Canny}$  that is contiguous to  $S_{LoG}$  at coordinates  $k$  and  $l$ . When  $E_{LoG}$  was less than  $E_{Canny}$  or when it was more than  $E_{Canny}$  and  $(n-m)$  was between 0 and threshold  $k_s$ ,  $S_{LoG}$  was gathered in  $f_{Hyb}$  and its contiguous  $S_{Canny}$  was ignored. Otherwise,  $S_{Canny}$  was gathered in  $f_{Hyb}$  and its contiguous  $S_{LoG}$  was ignored. Hence all the hybrid edges  $f_{Hyb}$  were acquired

by Eq. (14):

$$f_{Hyb}(a,b) = \begin{cases} S_{LoG}(i,j) | (a,b) = (i,j) & \text{if } (E_{LoG} < E_{Canny}) \\ S_{LoG}(i,j) | (a,b) = (i,j) & \text{if } (E_{LoG} > E_{Canny} \text{ and } 0 < n - m \leq k_s), \\ S_{Canny}(k,l) | (a,b) = (k,l) & \text{otherwise} \end{cases} \quad (14)$$

where  $S_{LoG}(i,j)$  is each segment of  $S_{LoG}$  at coordinates  $(i,j)$ ,  $S_{Canny}(k,l)$  is each segment of  $S_{Canny}$  that is contiguous to  $S_{LoG}(i,j)$  at coordinates  $(k,l)$ , and  $k_s$  is the threshold to protect the oversize of  $S_{LoG}$ . Finally, all of the hybrid edges,  $f_{Hyb}$ , were acquired for calculating the enhanced edge map in the next process. A sample image of hybrid edges is shown in Figure 4(d).

### Enhanced Gradient Vector Flow (EGVF)

The EGVF was composed of two stages: the first utilised an enhanced-edge map computation whilst the second was the EGVF field calculation.

#### Enhanced-edge map

The gradient magnitudes at the location of the hybrid-edge mask,  $f_{Hyb}$ , were enhanced while the other locations were kept unchanged. Then the enhanced gradient magnitude,  $f_e$ , was obtained by Eq. (15):

$$f_e(x,y) = \begin{cases} k_e \nabla(G(x,y) * I(x,y)) & \text{if } f_{Hyb}(x,y) = 1 \\ \nabla(G(x,y) * I(x,y)) & \text{otherwise} \end{cases} \quad (15)$$

where  $k_e$  is the weight for the gradient magnitude enhancement (in this case  $k_e=1.15$ , which was selected as the optimal result following the experimental increasing of the value in 0.01 increments),  $G(x,y)$  is the Gaussian filter,  $\nabla$  is the gradient operator and  $(x,y)$  are the coordinates of the image. The enhanced-edge map,  $f_{eh}$ , was then calculated from Eq. (16):

$$f_{eh}(x,y) = |f_e(x,y)|^2. \quad (16)$$

The enhanced-edge map preserved the gradient magnitude of real edges and decreased the gradient magnitude from noise. A sample image of an enhanced gradient magnitude is shown in Figure 5(c) and is different from the image obtained by the traditional gradient magnitude (Figure 5(b)) at the location where the hybrid edges are enhanced by the weight factor.

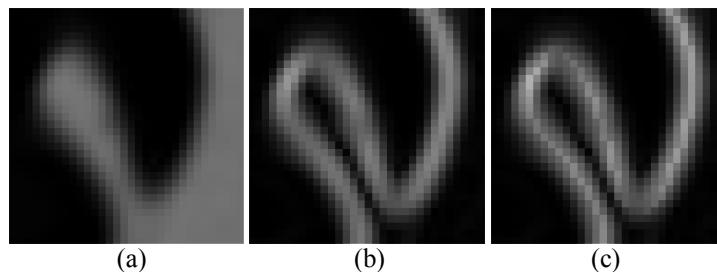


**Figure 5.** (a) Zoomed view image of square box of Figure 4(a); (b) traditional gradient magnitude of (a); (c) enhanced gradient magnitude of (a)

#### EGVF field

The EGVF field was obtained by applying the enhanced-edge map,  $f_{eh}$ , instead of the traditional edge map, as shown in Eq. (17):

$$V_t = \mu \nabla^2 V - (V - \nabla f_{eh}) |\nabla f_{eh}|^2, \quad (17)$$

where  $V_t$  is the partial derivative of  $V$  with respect to time  $t$ ,  $\mu$  is a regularisation parameter, and  $\nabla$  and  $\nabla^2$  are the gradient and Laplacian operators respectively. Then the EGVF deformable model was calculated and used to assist in pulling the curve towards the edge.

### Colon Segmentation and 3D Model Reconstruction

Colon segmentation was computed by utilising the connected component in 3D space. The largest volume was assumed to be the colon and the other organs were eliminated. In the case that the small intestine was inflated and connected with the colon, removal of the small intestine was performed by the anatomical knowledge that the small intestine is smaller but longer than the colon and that it connects to the colon at the cecum. Finally, the reconstructed 3D colon model was acquired by applying the marching cubes algorithm [32].

## RESULTS AND DISCUSSION

### Colon Cleansing

The proposed colon cleansing method was examined in three assessments by a radiologist based on the capability of the cleansing method and the confidence in its accuracy. The assessment criteria for the evaluation of the colon cleansing were achieved by the guidance of the expert radiologist. The first assessment evaluated the capability of eliminating the CEF at each position inside the colon in the CT images. Assigned scores (1 to 5) corresponded to percentage ranges of cleansing (0-25%, 26-50%, 51-75%, 75-99% and 100% respectively). The second assessment evaluated the accuracy of the region cleansing of the colon lumen and was rated from 1 to 4, where 1 = uninterpretable due to artefacts from faecal tagging, 2 = obvious wall irregularity, 3 = equivocal wall irregularity, and 4 = no wall irregularity. The third assessment evaluated the confidence in the accuracy of the colon cleansing technique and was scored from 1 to 3, for a low, moderate and high confidence level respectively. The mean scores of each data set for the above three assessments are shown in Table 1.

**Table 1.** Results of cleansing assessment

Data set	Score of colon cleansing (1 to 5)	Accuracy of region cleansing (1 to 4)	Confidence in image accuracy (1 to 3)
1	4.18 ± 1.58	3.37 ± 0.88	2.79 ± 0.41
2	4.80 ± 0.76	3.57 ± 0.81	2.91 ± 0.32
3	4.56 ± 1.25	2.92 ± 0.91	2.88 ± 0.32
4	4.82 ± 0.80	3.29 ± 0.90	2.90 ± 0.30

Note: Data are shown as mean ± 1SD. Data-set sizes are 1352, 1637, 945 and 1201 segments for data sets 1-4 respectively.

The assessment of the percentage of colon cleansing shows that all of the four data sets had a high percentage of cleansing and so the colon cleansing was satisfactory, with most of the CEF and PVE voxels being successfully removed regardless of their size and form (Figure 6). Even artefacts of inhomogeneous contrast-enhanced materials (mixture of contrast-enhancing agent and residual faeces) were eliminated (arrowed in Figures 6(j, m)) and the mucosa layer between air and soft tissue after cleansing was smooth and reconstructed. However, in the case that the patients did not follow the diet instruction prior to bowel preparation, the data sets might contain some tiny regions

of artefacts that sometimes could not be completely removed (arrowed in Figure 6(h)).

The assessment of accuracy of the region cleansing shows that three of the four data sets had satisfactory scores, with only one data set (no. 3) having a lower score, which was due to the problem of a beam hardening artefact that rendered the residual material incompletely enhanced. Hence the colon wall was not smooth (arrowed in Figure 6(n)).

Finally, the assessment of the confidence in the accuracy of the images shows that the proposed method is satisfactory and sufficient to assist the radiologist in diagnosing colorectal cancer and could be used in 3D colon reconstruction.

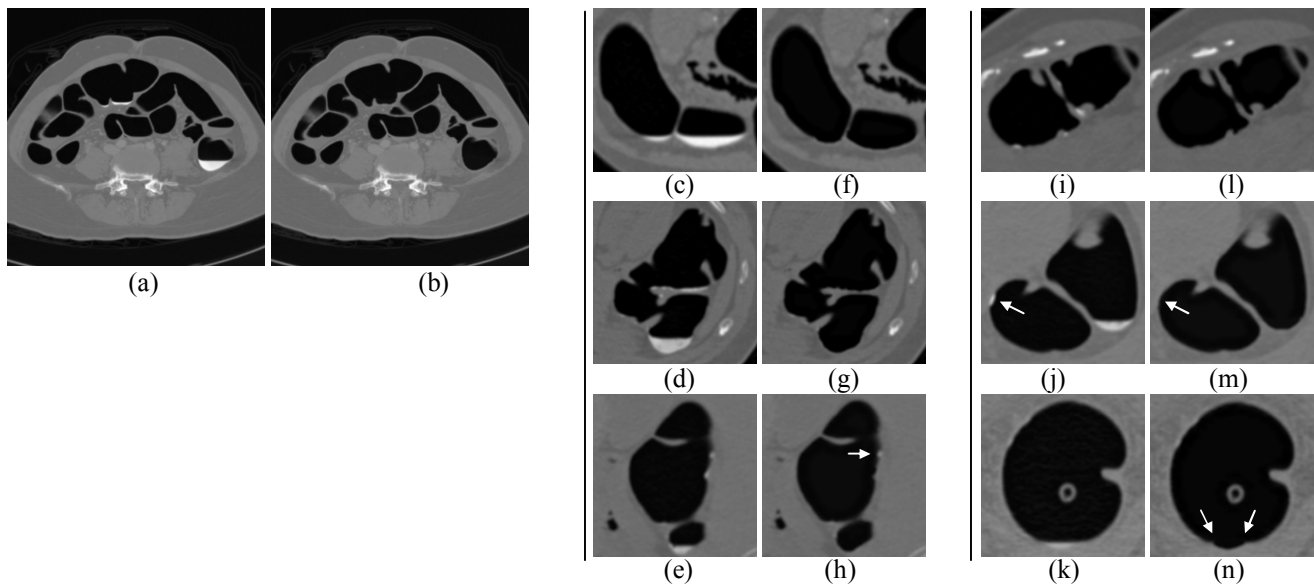


**Figure 6.** (a) CT image slice; (b) CT image after colon cleansing; (c-e, i-k) CT image slice (zoomed views); (f-h, l-n) corresponding CT image slice (zoomed views) after colon cleansing

The results of the comparison between the proposed cleansing method and the existing method of cleansing by threshold value selecting and vertical filter technique [4] are summarised in Figure 7. The existing methods produced a clear cleansed colon image when the selected threshold was 1,200 and 1,250 but they produced an oversegment on the CEF (square boxes in Figures 7(d, e, g, h)). When the selected threshold was slightly increased to 1,350, the oversegment was not found but instead it produced an undersegment on the CEF (square boxes in Figures 7(k, l)). Moreover, for all the selected threshold values operated with a vertical filter in the existing methods, the PVE of the interface layer between air and CEF that did not lie on the lower part of colon lumen due to gravity could not be removed (arrowed in Figures 7(f, i, l)). In contrast, the proposed cleansing method produced better results on removing the CEF and PVE from various image intensities and different locations of the CEF (Figures 7(m-o)), even if the CEF did not lie on the lower part of the colon lumen (arrowed in Figure 7(o)).

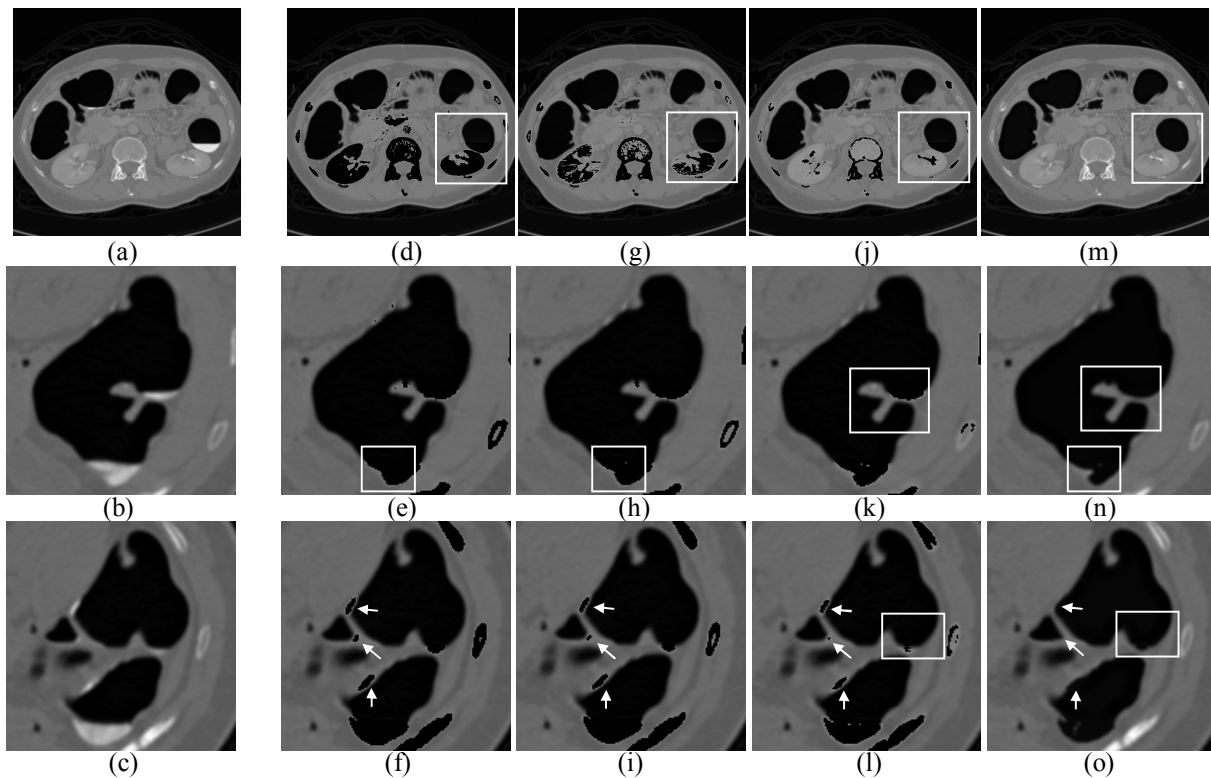


**Figure 7.** (a) CT image slice; (b, c) CT image slice (zoomed view); (d-l) CT image slice after colon cleansing by vertical filter method [4] with different thresholding values; (d-f) results from using threshold value = 1,200; (g-i) results from using threshold value = 1,250; (j-l) results from using threshold value = 1,350; (m-o) CT image slice after colon cleansing by proposed cleansing method

The intensity profiles along the cleaned colon lumen formed by the proposed cleansing method and those formed by the existing method of CEF and PVE voxel removal by threshold value selecting and vertical filter technique [4] are shown in Figure 8. Rapid intensity transitions along the cleaned colon wall were produced by the conventional method (Figure 8(a)), whereas the proposed cleansing method with mucosa layer reconstruction technique showed improvement in transitions of the intensity level of the colon lumen after colon cleansing (Figure 8(b)).

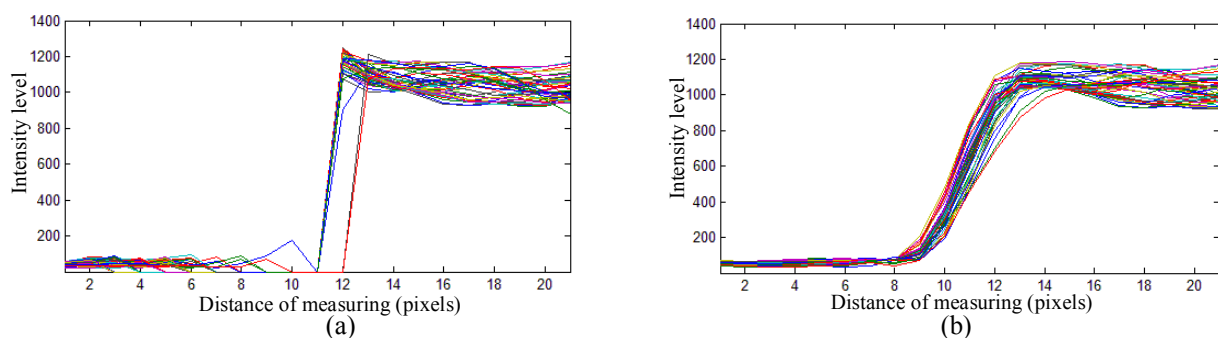


**Figure 8.** Intensity profiles of removed edge: (a) by selected threshold of 1,250 operated with vertical filter [4]; (b) by proposed cleansing method

### Colon-Wall Detection and Colon Segmentation

The proposed EGVF was developed to obtain a better detection of the colon-wall boundary compared with the traditional GVF. An example of the results with the same weight parameters are

shown in Figure 9. Although the traditional GVF method can detect a variety of colon wall shapes with a diminishing shaded intensity, it sometimes produces incomplete edges on the colon boundary (arrowed in Figures 9(e-h)), whereas the proposed EGVF gives a more complete edge pattern (arrowed in Figures 9(i-l)) with the shape almost like the colon segment from the CT image slice. When the automatically derived initial contours are misplaced, however, the EGVF and the GVF methods may fail to detect the thin tissue layers between the two segmented colon (arrowed in Figures 9(g, k)).

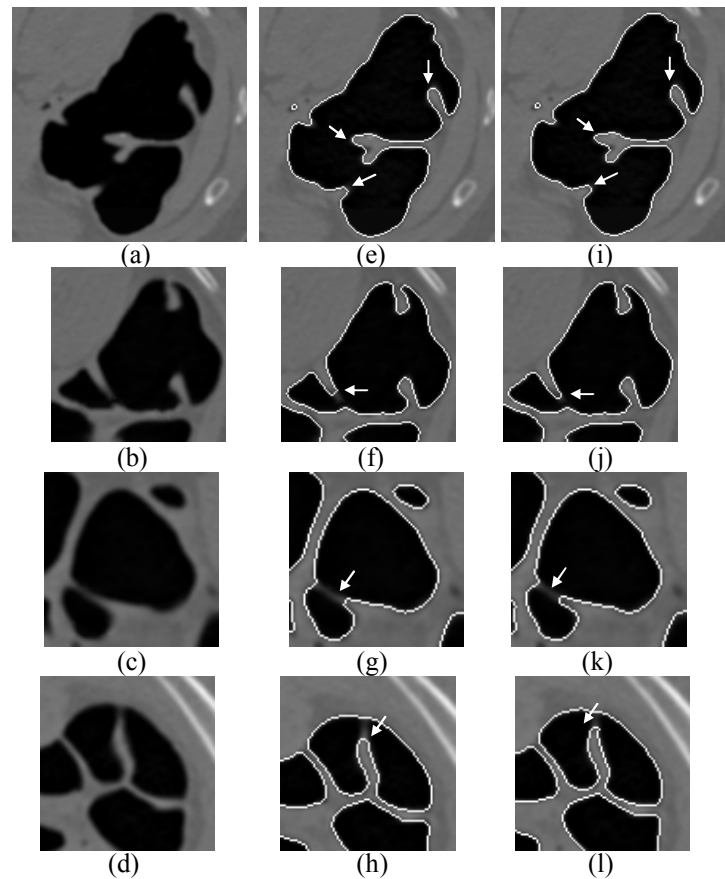


**Figure 9.** CT image slice (zoomed views) (a-d) and those after manipulation by GVF (e-h) and EGVF (i-l)

The performance of the proposed method for colon-wall detection and colon segmentation was compared with the existing segmentation methods of the watershed algorithm [10] and the level-set method [14]. The assessment was performed by comparing the results from all three techniques in terms of quality and accuracy of colon-wall detection, independently evaluated by two expert radiologists as a blind assessment—the radiologists did not know any information about the techniques which had been applied to each set of data. The assessment scores from the two radiologists were ranked on a scale from 1 (poor quality) to 10 (best quality), and in order to make the comparison reasonable, the initial contours from all techniques were automatically set in the same place by reference to the air inside the colon. The gradient magnitude and the standard deviation were used in the same range and the weight parameters of all techniques were increasingly adjusted in 0.01 increments and were selected from the best experimental results and employed to all data sets. For the proposed EGVF method, the weight parameters were  $\mu = 0.01$ ,  $\alpha =$

0.03,  $\beta = 0.01$  and  $k_e = 1.15$ . The EGVF deformable model algorithm was stopped if the area inside the deformable model in the last 10 iterations had no progress. This stopping condition was also applied to the level-set method. In addition to the original four data sets used previously (1-4), four more data sets (5-8) were examined so as to allow for differently-shaped colons.

The comparative assessment scores of the quality of the colon-wall detection on each data set from both radiologists for each technique, including the  $p$ -value by Duncan's multiple means tests, are summarised in Table 2. The proposed method clearly gave better results (numerically and statistically) on the detection of the colon wall than those from the other two traditional techniques (watershed and level-set methods) for all of the eight data sets examined, including their net means. That the means of all the assessment scores of the quality of colon-wall detection across all data sets did not numerically differ much between the three techniques may reflect the large number of segments of the colon.

**Table 2.** Assessment scores by watershed algorithm, level-set method and proposed EGVF of the quality of colon-wall detection of all colon segments

Data set	Radiologist 1				Radiologist 2			
	Watershed	Level set	EGVF	$p$ -value	Watershed	Level set	EGVF	$p$ -value
1	9.77 ± 0.79	9.74 ± 0.66	9.88 ± 0.45	5.13E <sup>-08*</sup>	9.94 ± 0.45	9.95 ± 0.28	9.99 ± 0.13	0.00035*
2	9.90 ± 0.49	9.91 ± 0.39	9.97 ± 0.19	3.56E <sup>-07*</sup>	9.89 ± 0.57	9.88 ± 0.43	9.98 ± 0.20	7.02E <sup>-12*</sup>
3	9.76 ± 0.89	9.87 ± 0.49	9.90 ± 0.35	3.80E <sup>-08*</sup>	9.78 ± 0.93	9.89 ± 0.45	9.94 ± 0.32	2.55E <sup>-07*</sup>
4	9.82 ± 0.96	9.91 ± 0.44	9.93 ± 0.37	1.14E <sup>-05*</sup>	9.88 ± 0.89	9.97 ± 0.23	9.99 ± 0.10	3.12E <sup>-07*</sup>
5	9.66 ± 1.31	9.80 ± 0.72	9.89 ± 0.51	1.25E <sup>-13*</sup>	9.87 ± 0.80	9.94 ± 0.35	9.98 ± 0.22	6.66E <sup>-10*</sup>
6	9.79 ± 1.02	9.93 ± 0.38	9.95 ± 0.30	5.39E <sup>-13*</sup>	9.86 ± 0.89	9.95 ± 0.33	9.98 ± 0.22	1.64E <sup>-09*</sup>
7	9.90 ± 0.59	9.91 ± 0.49	9.95 ± 0.40	0.00972*	9.96 ± 0.25	9.95 ± 0.22	9.99 ± 0.05	3.44E <sup>-11*</sup>
8	9.85 ± 0.68	9.89 ± 0.38	9.92 ± 0.32	0.00016*	9.92 ± 0.57	9.96 ± 0.24	9.99 ± 0.12	1.56E <sup>-07*</sup>
Mean	9.81 ± 0.53	9.87 ± 0.19	9.93 ± 0.16	6.19E <sup>-48*</sup>	9.89 ± 0.54	9.94 ± 0.21	9.98 ± 0.11	2.22E <sup>-50*</sup>

Note: Data are shown as mean ± 1 SD. Means followed by \* are significantly different at  $p < 0.01$  level (Duncan's multiple means test). Data-set sizes are 1352, 1637, 945, 1201, 1854, 1702, 1728 and 1661 segments for data sets 1-8 respectively.

In normal cases (segments without arrow in Figure 10), all techniques gave a broadly similar performance for the colon-wall segmentation. In special cases (segments with arrow in Figure 10), where the colon lumen had a small thin layer or a higher descending shaded intensity at the border of the colon lumen, however, each technique gave different results. The watershed algorithm could detect an obvious colon wall (Figure 10(h)), but it sometimes produced incomplete edges (arrowed in Figure 10(e)) and missed small tissue layers (arrowed in Figures 10(f, g)). Similarly, the level-set method could detect an explicit colon wall with a smooth curve (Figure 10(i)), but it could not move to the real shape with higher descending contrast intensity and concave regions (arrowed in Figures 10(j-l)). These could lead to false discrimination and misrepresent the size and shape of the colon-wall tissue layer, especially polyps. The EGVF gave a more completed edge (arrowed in Figures 10(m-p)) on capturing the concave regions, small tissue layers and colon boundary with diminishing shaded intensity.

With respect to the images from special conditions, segments of the colons were selected by both radiologists and then the comparative assessment scores of the quality of colon-wall detection for these special cases were analysed separately (Table 3). The mean assessment scores by both radiologists of the quality of the colon-wall detection in the selected special cases were all numerically and statistically better for the proposed method than the watershed and level-set

methods. Hence the proposed method seemed to give better results with various shapes of colon and even with special cases, except when the automatically allocated initial contours were misplaced, which resulted in rough edges.

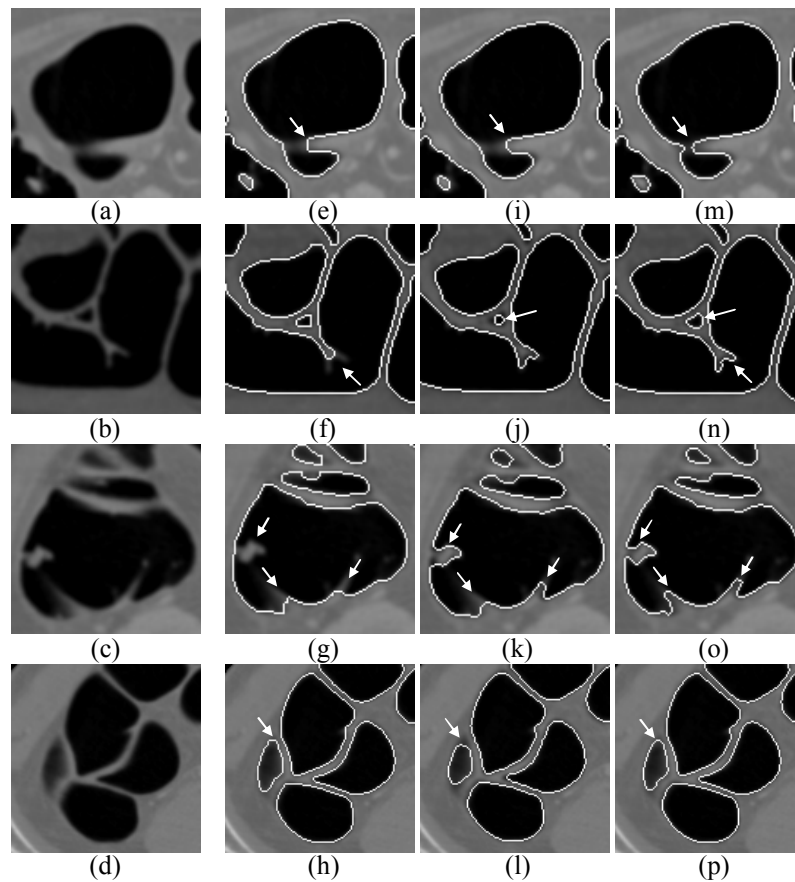


**Figure 10.** CT image slice (zoomed views) (a-d) and those after manipulation by watershed algorithm (e-h), level-set method (i-l) and EGVF (m-p)

**Table 3.** Assessment scores by watershed algorithm, level-set method and EGVF of quality of colon-wall detection in special cases

Data set	Radiologist 1				Radiologist 2			
	Watershed	Level set	EGVF	<i>p</i> -value	Watershed	Level set	EGVF	<i>p</i> -value
1	8.78 ± 1.46	8.62 ± 0.88	9.35 ± 0.84	9.78E <sup>-14*</sup>	9.70 ± 1.00	9.72 ± 0.59	9.93 ± 0.30	0.000179*
2	9.20 ± 1.18	9.26 ± 0.87	9.74 ± 0.48	8.06E <sup>-10*</sup>	9.09 ± 1.41	9.05 ± 0.86	9.83 ± 0.54	1.17E <sup>-16*</sup>
3	8.09 ± 1.80	8.92 ± 0.95	9.42 ± 0.83	7.45E <sup>-14*</sup>	8.26 ± 2.09	9.08 ± 0.94	9.52 ± 0.78	1.14E <sup>-10*</sup>
4	7.33 ± 2.59	8.73 ± 1.10	9.02 ± 1.00	9.27E <sup>-10*</sup>	8.27 ± 2.95	9.53 ± 0.77	9.92 ± 0.36	1.17E <sup>-08*</sup>
5	7.01 ± 2.73	8.25 ± 1.35	9.05 ± 1.21	4.10E <sup>-25*</sup>	8.82 ± 2.10	9.49 ± 0.94	9.80 ± 0.81	9.27E <sup>-12*</sup>
6	7.30 ± 2.60	9.04 ± 1.01	9.30 ± 0.86	8.57E <sup>-22*</sup>	8.21 ± 2.72	9.36 ± 1.01	9.73 ± 0.74	4.89E <sup>-12*</sup>
7	8.85 ± 1.64	9.04 ± 1.33	9.41 ± 1.21	0.00169*	9.61 ± 0.76	9.47 ± 0.54	9.97 ± 0.18	8.03E <sup>-15*</sup>
8	8.63 ± 1.63	9.02 ± 0.71	9.28 ± 0.70	2.13E <sup>-07*</sup>	9.26 ± 1.61	9.66 ± 0.64	9.91 ± 0.37	1.48E <sup>-08*</sup>
Mean	8.25 ± 2.11	8.84 ± 1.09	9.34 ± 0.94	6.50E <sup>-76*</sup>	9.03 ± 1.88	9.44 ± 0.82	9.84 ± 0.56	9.14E <sup>-61*</sup>

Note: Data are shown as mean ± 1 SD. Means followed by \* are significantly different at the  $p < 0.01$  level (Duncan's multiple means test). Data-set sizes are 257, 199, 118, 83, 209, 132, 157 and 179 segments for data sets 1-8 respectively.

In the final process the colon segmentation was performed based on anatomical structures and volume analysis, and the contiguous small intestine was removed. Then the surface rendering was performed to finally reconstruct the 3D colon model (Figure 11). The average time for each step is shown in Table 4; all calculations were performed in Matlab environment on Windows 7 using a PC computer with a 2.0GHz Core i7 processor and 4 GB of RAM memory.



**Figure 11.** 3D model of the colon

**Table 4.** Average time for each step for a 512×512-voxel CT image size

Processing step	Time (second)	Time (%)
<i>Colon cleansing</i>		
Elimination of area outside abdomen	0.0957	1.3760
Image sharpening by Laplacian operator	0.0446	0.6413
K-means clustering for colon classification	1.1349	16.3180
Lungs removal	0.0411	0.5910
Automatic CEF and PVE segmentation	0.7563	10.8743
Colon cleansing and mucosa reconstruction	0.0897	1.2897
<i>Colon-wall detection and colon segmentation</i>		
Canny edge detection with automatic threshold setting	0.1188	1.7081
LoG detection with automatic threshold setting	0.0793	1.1402
Hybrid edge construction	0.0604	0.8685
EGVF for colon-wall detection and colon segmentation	4.5341	65.1929
Total	6.9549	100

## CONCLUSIONS

In our hybrid framework for reconstructing a 3D colon model, the accuracy of the colon cleansing was satisfactory. All PVE and CEF were successfully removed and the mucosal layer was reconstructed just like in the natural colon lumen. Some troubles with the tiny artefacts were overcome by applying more features to extract. The accuracy of the colon-wall detection was better than the conventional watershed and level-set methods. The limitation imposed by misplaced initial contours could be improved by adding more features to adapt contours. The 3D model of the colon was successfully reconstructed and sufficient for the radiologist's diagnostic examinations.

## ACKNOWLEDGEMENTS

The authors thank the Department of Radiology, Chulalongkorn University for providing the CT image data sets. We also thank Sareeya Ruamsup MD and Sumunta Thongtong MD for their helpful suggestions and discussions. Dr. Robert Butcher from the Publication Counselling Unit, Chulalongkorn University is thanked for comments on the manuscript and English proofreading.

**REFERENCES**

1. R. Nishihara, K. Wu, P. Lochhead, T. Morikawa, X. Liao, Z. R. Qian, K. Inamura, S. A. Kim, A. Kuchiba, M. Yamauchi, Y. Imamura, W. C. Willett, B. A. Rosner, C. S. Fuchs, E. Giovannucci, S. Ogino and A. T. Chan, “Long-term colorectal-cancer incidence and mortality after lower endoscopy”, *N. Engl. J. Med.*, **2013**, *369*, 1095-1105.
2. J. P. Heiken, C. M. Peterson and C. O. Menias, “Virtual colonoscopy for colorectal cancer screening: Current status”, *Cancer Imaging*, **2005**, *5*, S133-S139.
3. S. Wang, L. Li, H. Cohen, S. Manke, J. J. Chen and Z. Liang, “An EM approach to MAP solution of segmenting tissue mixture percentages with application to CT-based virtual colonoscopy”, *Med. Phys.*, **2008**, *35*, 5787-5798.
4. K. Y. Chang, H. H. Zhang, S. J. Chen, L. S. Chen and J. H. Chen, “Automatic colon segmentation using isolated-connected threshold”, Proceedings of 1st International Conference on Robot, Vision and Signal Processing, **2011**, Kaohsiung, Taiwan, pp.44-47.
5. G. Slabaugh, X. Yang, X. Ye, R. Boyes and G. Beddoe, “A robust and fast system for CTC computer-aided detection of colorectal lesions”, *Algorithms*, **2010**, *3*, 21-43.
6. A. Skalski, M. Socha, T. Zieliftski and M. Duplaga, “Colon cleansing for virtual colonoscopy using non-linear transfer function and morphological operations”, Proceedings of 7th IEEE International Workshop on Imaging Systems and Techniques, **2007**, Krakow, Poland, pp.1-5.
7. V. Bevilacqua, M. Cortellino, M. Piccinni, A. Scarpa, D. Taurino, G. Mastronardi, M. Moschetta and G. Angelelli, “Image processing framework for virtual colonoscopy”, Proceedings of 5th International Conference on Intelligent Computing, **2009**, Ulsan, South Korea, pp.965-974.
8. J. H. Bidgoli, A. Ahmadian, S. Akhlagpor, N. R. Alam and S. Z. Mahmoodabadi, “An efficient colon segmentation method for oral contrast-enhanced CT colonography”, Proceedings of 2005 IEEE Engineering in Medicine and Biology 27<sup>th</sup> Annual Conference, **2005**, Shanghai, China, pp.3429-3432.
9. M. Ismail, S. Elhabian, A. Farag, G. Dryden and A. Seow, “Fully automated 3D colon segmentation for early detection of colorectal cancer based on convex formulation of the active contour model”, Proceedings of IEEE Computer Vision and Pattern Recognition Workshops, **2012**, Providence, Rhode Island, pp.58-63.
10. A. Skalski, M. Socha, T. Zieliftski and M. Duplag, “Virtual Colonoscopy - Technical Aspects”, in “Colonoscopy” (Ed. P. Miskovitz), InTech, Rijeka (Croatia), **2011**, Ch.17.
11. W. Cai, J. G. Lee, M. E. Zalis and H. Yoshida, “Mosaic decomposition: An electronic cleansing method for inhomogeneously tagged regions in noncathartic CT colonography”, *IEEE Trans. Med. Imaging*, **2011**, *30*, 559-574.
12. S. Tan, J. Yao, M. M. Ward and R. M. Summers, “Linear measurement of polyps in CT colonography using level sets on 3D surfaces”, Proceedings of IEEE Engineering in Medicine and Biology Society, **2009**, Minneapolis, USA, pp.3617-3620.
13. D. Chen, H. Abdelmunim, A. A. Farag, R. Falk and G. Dryden, “Segmentation of colon tissue in CT colonography using adaptive level sets method”, Proceedings of MICCAI 2008 Workshop on Computational and Visualization Challenges in the New Era of Virtual Colonoscopy, **2008**, New York, USA, pp.108-115.
14. K. Chunhaponpipat, L. Vajragupta, B. Chaopathomkul, N. Cooharajanone and R. Lipikorn, “Automatic colon cleansing in CTC image using gradient magnitude and similarity measure”, *SIP Comm. Comp. Inform. Sci.*, **2009**, *61*, 82-89.

15. H. Zhu, M. Barish, P. Pickhardt and Z. Liang, "Haustal fold segmentation with curvature-guided level set evolution", *IEEE Trans. Biomed. Eng.*, **2013**, *60*, 321-331.
16. M. Kass, A. Witkin and D. Terzopoulos, "Snakes: Active contour models", *Int. J. Comput. Vision*, **1988**, *1*, 321-331.
17. C. Xu and J. L. Prince, "Snakes, shapes, and gradient vector flow", *IEEE Trans. Image Process.*, **1998**, *7*, 359-369.
18. B. Chen, J. Zhao, E. Dong, J. Chen, Y. Zhao and Z. Yuan, "An improved GVF snake model using magnetostatic theory", Proceedings of Computer, Informatics, Cybernetics and Applications, **2012**, Hangzhou, China, pp.431-440.
19. H. Zhou, X. Li, G. Schaefer, M. E. Celebi and P. Miller, "Mean shift based gradient vector flow for image segmentation", *Comput. Vis. Image Und.*, **2013**, *117*, 1004-1016.
20. T. K. Chuah, C. W. Lim, C. L. Poh and K. Sheah, "Bone segmentation of magnetic resonance images by gradient vector flow active contour with atlas based centroid forces", Proceedings of International Conference on Digital Image Computing: Techniques and Applications, **2010**, Sydney, Australia, pp.126-131.
21. S. Choi and C. Kim, "Automatic initialization active contour model for the segmentation of the chest wall on chest CT", *Healthcare Inform. Res.*, **2010**, *16*, 36-45.
22. A. M. Kop and R. Hegadi, "Kidney segmentation from ultrasound images using gradient vector force", *Int. J. Comput. Appl.*, **2010**, *2*, 104-109.
23. M. K. A. Mahmoud and A. Al-Jumaily, "Segmentation of skin cancer images based on gradient vector flow (GVF) snake", Proceedings of International Conference on Mechatronics and Automation, **2011**, Beijing, China, pp.216-220.
24. S. Patil, V. R. Udipi and D. Patole, "A robust system for segmentation of primary liver tumor in CT images", *Int. J. Comput. Appl.*, **2013**, *75*, 6-10.
25. P. M. Patel, B. N. Shah and V. Shah, "Image segmentation using K-mean clustering for finding tumor in medical application", *Int. J. Comput. Trends Technol.*, **2013**, *4*, 1239-1242.
26. J. Canny, "A computational approach to edge detection", *IEEE Trans. Pattern Anal. Mach. Intell.*, **1986**, *8*, 679-698.
27. D. Marr and E. Hildreth, "Theory of edge detection", *Proc. R. Soc. Lond. B*, **1980**, *207*, 187-217.
28. R. C. Gonzalez and R. E. Woods, "Digital Image Processing", 2nd Edn., Prentice Hall, Englewood Cliffs, **2002**, pp.45-56.
29. M. Basu, "Gaussian-based edge-detection methods—A survey", *IEEE Trans. Syst. Man Cybern. C*, **2002**, *3*, 252-260.
30. M. Roushdy, "Comparative study of edge detection algorithms applying on the gray scale noisy image using morphological filter", *Int. J. Graphics Vis. Image Process.*, **2006**, *6*, 17-23.
31. M. Bennamoun, B. Boashash and J. Koo, "Optimal parameters for edge detection", Proceedings of IEEE International Conference on Systems, Man and Cybernetics, 1995. Intelligent Systems for the 21<sup>st</sup> Century, **1995**, Vancouver, Canada, Vol. 2, pp.1482-1488.
32. W. E. Lorensen and H. E. Cline, "Marching cubes: A high resolution 3D surface construction algorithm", *ACM SIGGRAPH Comp. Graphics*, **1987**, *21*, 163-169.